International Journal of Heat and Mass Transfer 176 (2021) 121484

Contents lists available at ScienceDirect

International Journal of Heat and Mass Transfer

journal homepage: www.elsevier.com/locate/hmt

# The effect of condenser temperature on the performance of the evaporator in a wickless heat pipe performance

Jiaheng Yu[a], Thao T.T. Nguyen[a], Anisha Pawar[a], Peter C. Wayner Jr.[a], Joel L. Plawsky[a,*], David F. Chao[b], Ronald J. Sicker[b]

[a] The Howard P. Isermann Department of Chemical and Biological Engineering, Rensselaer Polytechnic Institute, Troy, NY, 12180, USA
[b] NASA Glenn Research Center, Cleveland, OH, 44135, USA

ARTICLE INFO

*Article history:*
Received 15 February 2021
Revised 21 April 2021
Accepted 11 May 2021

*Keywords:*
Heat pipe
Marangoni flow
Energy performance
Condenser temperature
Condensation
Capillarity

ABSTRACT

The Constrained Vapor Bubble (CVB), a simple, wickless, heat pipe design that depends on interfacial forces to drive corner flow in a square cuvette, was studied in the microgravity environment aboard the International Space Station (ISS). In this paper, we consider the effects of different condenser temperatures on the heat transfer and fluid flow behavior using pentane as the working fluid. As the condenser temperature was decreased, the performance of the system decreased. This performance decrease using the pure working fluid was opposite to the behavior observed when using a mixture of 94 vol% pentane and 6 vol% isohexane. The mechanism for the decline in performance as the condenser temperature was lowered was a stronger than expected increase in the apparent strength of Marangoni flows at the heater end of the system. A simple mathematical model was fit to the experimental data and used to extract an evaporator heat transfer coefficient for experiments where we held the condenser temperature constant while increasing the heater power and where we held the heater power constant while decreasing the condenser temperature. All the results could be collapsed onto a single Nusselt number vs. Marangoni number curve. In this formulation, the Nusselt number was found to decrease with increasing Marangoni number to the 1/3 power.



## 1. Introduction

Heat pipes are designed to assist in removing heat from the hot spot of a device and dissipating that heat to the surrounding environment. Evaporation of the working liquid removes heat from the hot end. The vapor flows to the cold end where it condenses and releases heat to the environment through a heat sink attached to the condenser. The condensed liquid returns to the hot end via capillary forces, so no mechanical pumping is required. This cycle of evaporation, condensation, and liquid return is repeated indefinitely, leading to many applications for the technology [1–4].

The development of the heat pipe has a long history, and scientists have done extensive studies both analytically and experimentally, on a large variety of different heat pipe configurations [5–16]. The effects of evaporation and condensation on the performance of heat pipes have been studied, and numerical models have been constructed to analyze the impact of phase change on the heat transfer performance [1–4]. In general, the experiments and models agree, especially in a terrestrial environment. Transparent, wickless systems, designed to better understand the dynamics of phase change in the liquid meniscus, contact line region, and thin film regions have also been studied experimentally [17] and modeled [18]. The behavior of the heat flux profile and its dependence on the meniscus curvature has been analyzed using heat transfer models and optical interferometry to measure the film thickness profile in the device [18].

In terrestrial applications, the three primary forces driving the performance of a heat pipe are gravity, fluid friction, and capillarity. In the absence of gravity, Marangoni forces that arise due to surface tension gradients, become important factors driving fluid flow [19,20]. In a wickless heat pipe, the capillary force driving liquid flow is a function of the contact angle the liquid makes with the solid surface and the corner angle along which the liquid flows [21–23]. As the corner angle becomes more acute, the capillary force increases but the frictional losses for liquid flowing along that corner also increase. Dry-out of the hot end of the heat pipe happens when the evaporation rate and the frictional and Marangoni forces combine to exceed the capillary force avail-

* Corresponding author.
*E-mail addresses:* yuj10@rpi.edu (J. Yu), nguyen.thaoche@gmail.com (T.T.T. Nguyen), pawara@rpi.edu (A. Pawar), wayner@rpi.edu (P.C. Wayner Jr.), plawsky@rpi.edu (J.L. Plawsky), david.f.chao@nasa.gov (D.F. Chao), ronald.j.sicker@nasa.gov (R.J. Sicker).

https://doi.org/10.1016/j.ijheatmasstransfer.2021.121484
0017-9310/

**Nomenclature**

*Roman symbols*

| | |
|---|---|
| $A_c$ | cross sectional area of the cuvette wall ($m^2$) |
| $Bo$ | Bond number |
| $g$ | gravitational acceleration ($m/s^2$) |
| $h_{in}$ | average internal heat transfer coefficient ($W/m^2$ K) |
| $k$ | thermal conductivity (W/m K) |
| $L$ | characteristic length (m) |
| $Ma$ | Marangoni number |
| $Nu$ | Nusselt number |
| $P$ | measured pressure at each cooling setting (Pa) |
| $P_{in}$ | inside perimeter of the cuvette (m) |
| $P_{out}$ | outside perimeter of the cuvette (m) |
| $q_{cond}$ | conduction heat transfer rate (W) |
| $q_{out,rad}$ | thermal radiation heat transfer rate (W) |
| $q_{in}$ | internal heat transfer rate (W) |
| $q'_{cond}$ | conduction heat flow per unit length (W/m) |
| $q'_{out,rad}$ | outside radiation heat flow per unit length (W/m) |
| $q'_{in}$ | internal heat transfer flow per unit length (W/m) |
| $T$ | temperature (K) |
| $TC_n$ | the $n^{th}$ thermocouple |
| $T_v$ | temperature of the vapor (K) |
| $T_\infty$ | temperature of the external environment (K) |
| $x$ | distance (m) |

*Greek symbols*

| | |
|---|---|
| $\alpha$ | thermal diffusivity of the liquid ($m^2/s$) |
| $\varepsilon$ | emissivity of the cuvette material |
| $\mu$ | dynamic viscosity of the liquid (N s/$m^2$) |
| $\rho$ | density ($kg/m^3$) |
| $\sigma$ | Stefan–Boltzmann constant ($W/m^2$ $K^4$) |
| $\sigma_l$ | surface tension of the liquid (N/m) |

able for pumping the liquid back from the condenser end [24,25]. V-shaped angular heat pipe experiments have been conducted to study this dry-out limitation, and numerical models were developed to evaluate the capillary limit and heat transfer at the meniscus [26–30].

Our group has analyzed the effects of using a binary mixture of 94 vol% pentane and 6 vol% isohexane as the working fluid in microgravity in an attempt to minimize the effect of Marangoni forces [31]. The study showed that changes in the liquid phase composition could offset the temperature-induced Marangoni stresses that develop near the heater end and thereby increase the heat transfer coefficient at the evaporator end of the device. The study also investigated changing the temperature at the condenser end of the device while holding the heat input constant. An increase in the heat transfer coefficient in the evaporation region was correlated with a decrease in the condenser temperature even though the two ends were roughly 40 mm apart.

We recently uncovered a similar set of experiments that were run prior to the mixture experiments using pure pentane as the working fluid. In this article, we analyze the pure fluid case using a simple, one-dimensional heat transfer model in combination with detailed images of the liquid-vapor interface to understand why the behavior of the pure system was so much different than that for the mixture and why decreasing the condenser temperature had a similar effect to increasing the heater power input. Distinct regions of the heat pipe were identified based on their visual characteristics and thermodynamic properties. The extent of these regions and the effective heat pipe length were compared at different condenser temperature settings. Bowman and Maynes, using an analytical analysis, showed that lower temperatures at the condenser end enhanced the average internal heat transfer coefficient of the heat pipe [32]. However, by considering the effect of Marangoni stress, we found both the area over which condensation occurred and the internal heat transfer coefficient decreased with decreasing condenser temperature and adversely affected heat pipe performance.

### 1.1. Experimental apparatus

The experimental apparatus included a fused silica cuvette, which served as a transparent wickless heat pipe. An image captured by a surveillance camera for the experiment is shown in Fig. 1a. The outside cross section of the cuvette is 5.5 × 5.5 mm, and the inside channel is 3.0 × 3.0 mm. Pure pentane was used as the working fluid and partially filled the cuvette to achieve a desired bubble length. The experimental system was operated aboard the International Space Station in the Fluids Integrated Rack. The rack contained the Light Microscopy Module that was used for the optical observations. Heating and cooling of the cuvette were achieved by installing an electrical resistance heater and a cold finger attached to several thermoelectric coolers respectively at the two ends of the heat pipe. In this article, we focus on a discussion of the 40 mm version of the device. 40 mm represents the length of the vapor bubble in the system. The condenser end was kept at a constant temperature during each run, while the heat input was maintained at 2.0 W. Four condenser temperature settings, 25°C, 19°C, 10°C, and -5°C, were applied to study their effect on the heat pipe performance. The temperature profile along the main axis of the device was recorded by type-E thermocouples installed on one side of the cuvette wall, and the steady-state temperatures of the last 20 measurements were averaged for analysis. The thermocouples used in the experiment have a specified accuracy of ± 0.5 K. The heater and the condenser temperatures were also monitored and measured by thermocouples. The internal pressure was measured using a pressure transducer with an accuracy of ± 0.69 kPa. Similarly, the last 20 measurements of the pressure at the steady-state were averaged to reduce the noise and enhance the accuracy. A more detailed description of the experiment operations can be found in previous publications [10,11,18,31].

## 2. Results and discussion

The constrained vapor bubble experiment was conducted on the International Space Station to minimize the influence of gravity. The goal was to achieve a very low Bond number, *Bo*, by exposing the system to a gravitational acceleration, *g*, equal to 0.19 $\mu g$.

Four experimental condenser runs are discussed in this article, and each was conducted using a constant heater power of 2.0 ± 0.01 W. The condenser temperature was varied from a high of 25°C to a low of -5°C. The temperature profiles along the main axis of the heat pipe for these four runs are shown in Fig. 1b. An isothermal region of varying length is observed in the middle of the heat pipe for each run. The length of that region decreased as the condenser temperature decreased. The internal pressure of the cuvette for these conditions is shown in Fig. 1c. The pressure decreased by as much as ~30% as the condenser temperature decreased.

A full view of the cuvette was available using a wide-angle, surveillance camera as shown in Figs. 1a and 2a. A microscope was used to capture a series of images at 10× magnification shown in Fig. 2b, and these images were stitched together to provide more detailed information of the fluid flow and the liquid film thickness in the heat pipe as shown in Fig. 2c.

Generally, a heat pipe can be separated into three distinct zones according to the dominant heat transfer process occurring there:

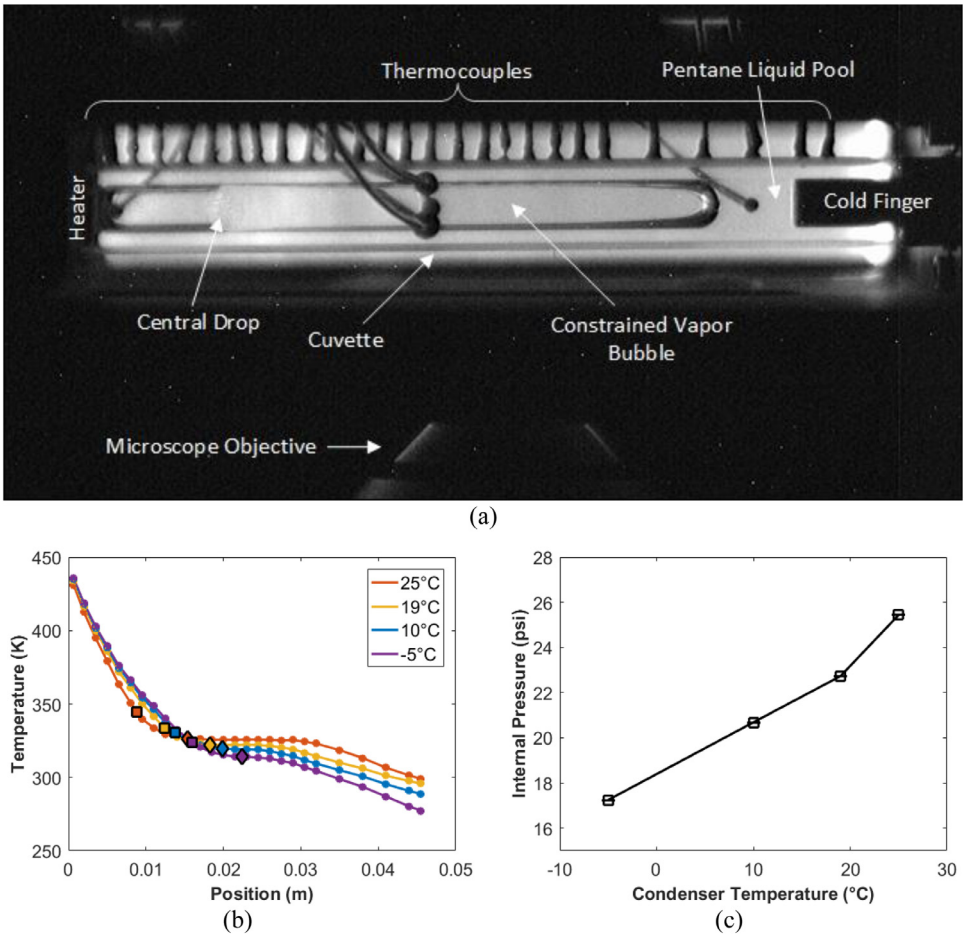


**Fig. 1.** (a) A surveillance image taken at low magnification showing the experimental apparatus of the 40-mm-long fused silica heat pipe module. (b) The temperature profiles along the main axis of the 40 mm heat pipe as a function of the condenser temperature at the cold end. The solid squares represent the central drop location; the solid diamonds represent the transition between the evaporation and the condensation regions. The error of each temperature measurement is small, ± 0.5 °C, and represents the standard error of the last 20 measurements for each case under steady state condition. (c) The internal cuvette pressure measurements at different condenser temperature settings. Error bars, that are only as big as the symbols, represent the standard error of the last 20 measurements for each case under steady state conditions.

an evaporation region, an adiabatic region, and a condensation region. However, because the system used here is transparent and its outer surface is exposed to the environment, the adiabatic region is replaced by an isothermal region as seen in Fig. 1b. We treat this heat pipe as a combination of three regions based on the distinctive visual characteristics of the liquid-vapor interface, as demonstrated in Fig. 2b. Region I is defined as the interfacial flow region and covers a section from the heater end to where a central drop appears. The temperature gradients between the heater end and the central drop for all four runs are greater than 7000 K/m. At such high temperature gradients, significant Marangoni stresses can develop at the liquid-vapor interface and induce a flow of liquid away from the higher temperature locations. The sharp corners of the wickless cuvette enable a capillary flow that drives the liquid from the condenser end to the heater end. The two opposing flows form a local, thick, liquid drop that spreads over the flat surface. We termed this phenomenon a flooding limitation in previous publications [33–36]. Region II represents an evaporation zone that spans an area from the central drop until the position where the flat surface of the heat pipe reaches the saturation temperature of the vapor and starts to be covered by a condensate film. This last portion of the cuvette, Region III, is defined as the condensing region.

In Fig. 1b, the slopes of the temperature profiles near the heater end for all four condenser settings are all negative and the magnitude of the slope near the heater end decreases with decreasing condenser temperature. This is expected as the heat load into the device is constant but the overall, end-to-end driving force for heat transfer increases. As the slope near the heater end decreases with decreasing condenser temperature, the isothermal region also shrinks to the point where it nearly disappears at the lowest condenser temperature setting. The isothermal region exists due to a balance between condensation on the inner surface of the heat pipe and heat rejection to the surroundings. As the condenser temperature drops, the internal pressure drops, condensation starts closer to the condenser itself and the extent of the isothermal region correspondingly shrinks and eventually nearly disappears. The surveillance images in Fig. 2a and the 10× composite images in Fig. 2c illustrate that the interfacial flow region grows tremendously as the condenser temperature decreases extending to over 1/3 of the length of the device at the lowest condenser temperature. The thick, liquid film in this region limits the amount of evaporation that can occur, and so, as the region grows, the performance of the heat pipe decreases. Previous work using a constant condenser temperature and a variable heat input reported similar behavior [35]. This phenomenon was also directly related to the growth of the interfacial region. We attribute this to Marangoni forces and attempt to quantify it below.

A one-dimensional analytical model was developed to support the observations in Figs. 1 and 2. It serves to define a set of in-

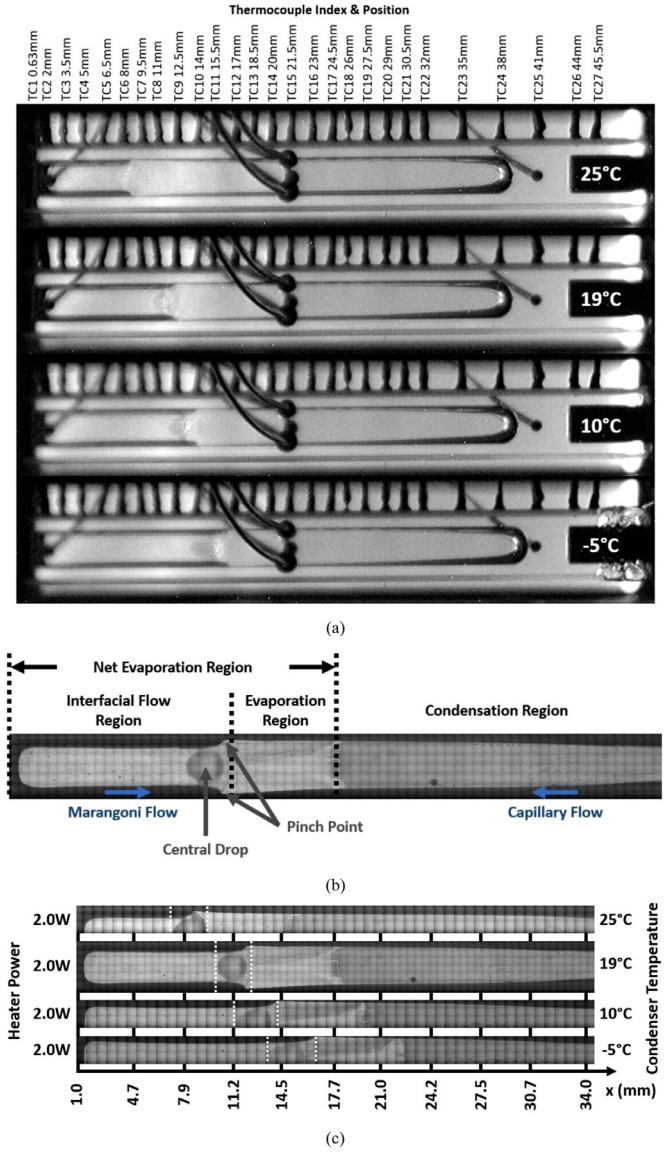


**Fig. 2.** (a) Surveillance images of the 40 mm system with the same heater power input but at various condenser temperature settings. Labels indicate the numbering sequence for the thermocouples and their locations along the cuvette main axis. (b) A composite, 10× image of the 40 mm device at 2.0 W heater input and 19°C condenser temperature. The heat pipe is segmented into three distinct regions based on the dominant thermal-fluid processes occurring. (c) 10× composite images of the liquid distribution for different condenser temperature settings. The dashed lines enclose the span of the central drop.

ternal heat transfer coefficients that we can correlate with the images and interfacial phenomena we observe inside the device. The model is similar to that of Bowman and Maynes [32]. Due to the microgravity environment aboard the ISS, natural convection about the outer surface was negligible. Thus, the model was based on the following three heat transfer mechanisms: conduction of heat within the glass wall of the cuvette along the main heat transfer axis ($q_{cond}$); radiative heat exchange between the cuvette external surfaces and its surrounding environment ($q_{out,rad}$); and convective heat transfer internal to the heat pipe that accounts for phase change and single-phase flow components ($q_{in}$). Fig. 3 demonstrates, schematically, these three mechanisms within the control volume of the wickless heat pipe.

An energy balance was constructed based on the control volume shown in Fig. 3. This led to the following, simplified differential equation:

$$kA_c\frac{d^2T}{dx^2} - \underbrace{P_{in}h_{in}(T - T_v)}_{q'_{in}} - \sigma\varepsilon P_{out}\left(T^4 - T_\infty^4\right) = 0 \quad (1)$$

where $T_\infty$ represents the temperature of the external environment, which is 21°C on average and measured by thermocouples in the external housing where the cuvette was mounted. A derivation of this equation can be found in Appendix 1. $P_{in}$ is the inside perimeter of the heat pipe, $P_{out}$ is the external perimeter, and $T_v$ is the saturation temperature of the working fluid in the vapor phase. $h_{in}$ is an average, internal heat transfer coefficient and $q'_{in}$ is the heat flow per unit length into or out of the internal walls of our device.

To solve for $h_{in}$, the only unknown variable in Eq. (1) is $T_v$, the vapor temperature. However, we can calculate the value of $T_v$ by setting Eq. (2) to be zero. $q'_{in} = 0$ here represents the point where we transition from net evaporation to net condensation.

$$q'_{in} = q'_{cond} + q'_{out,\ rad} \quad (2)$$

The vapor temperature, $T_v$, is assumed to be relatively constant throughout the cuvette and setting Eq. (2) to zero yields a temperature very close to the experimentally measured temperature at which condensation starts to appear on the walls of the cell.

The temperature profiles for all four experimental runs were fitted with 6$^{th}$ degree polynomials. The order of the polynomial provided a good fit to the data while still being smooth enough to differentiate. The polynomial was used to evaluate each term in Eq. (1) and determine $q'_{in}$. This is shown in Fig. 4a. $q'_{in} < 0$ represents regions where heat was being removed from the wall, and $q'_{in} > 0$ indicates regions where heat is being deposited onto the wall. The last three data points in each curve represent the heat transfer occurring in the region near the condenser. The behavior of $q'_{in}$ near the condenser changes sign because the condenser was set at a temperature above the dew point (25°C), near the dew point (19°C), below the dew point (10°C), and below the frost point (-5°C) respectively on the space station.

We see in Fig. 4a, the rate of internal heat transfer, $q'_{in}$, switches sign from positive to negative in the region close the heater end, which indicates a change from heat gain by the wall (condensation) to heat loss from the wall (evaporation). The $q'_{in}$ profile of Fig. 4a also exhibits a local mathematical minimum that corresponds to a maximum in the evaporative heat transfer rate. This minimum occurs where the competing Marangoni and capillary flows meet. The local minimum in $q'_{in}$ moves away from the heater end as the condenser temperature is lowered and tracks the motion and extent of the interfacial region.

Fig. 4a shows the boundary between the net evaporation and the net condensation regions represented by the second occurrence where $q'_{in} = 0$. This point also moves further away from the heater end as the condenser temperature decreased and the position of this boundary was used to evaluate $T_v$.

Fig. 4b compares the results of finding the location of the central drop using the analytical model, $q'_{in} = 0$, and the 10× magnification images. The 10× images have a resolution of 1.3 $\mu$m per pixel. Hence, the position and the distance of the central drop from the heater wall could be measured by counting the number of pixels involved and then multiplying by the length of a pixel. From Fig. 4b, the local minimum of $q'_{in}$ is also able to reproduce the trend of the central drop movement with the variation of the condenser temperature. As shown in Fig. 4c, the vapor temperature estimated from the regression model, $q'_{in} = 0$ decreases with a decrease in the condenser temperature.

The polynomial regression model was subject to two additional verification methods to ensure the estimate of $T_v$ was accurate enough to extract an average heat transfer coefficient. Using the measured internal pressure and the Antoine equation, Eq. (3), we

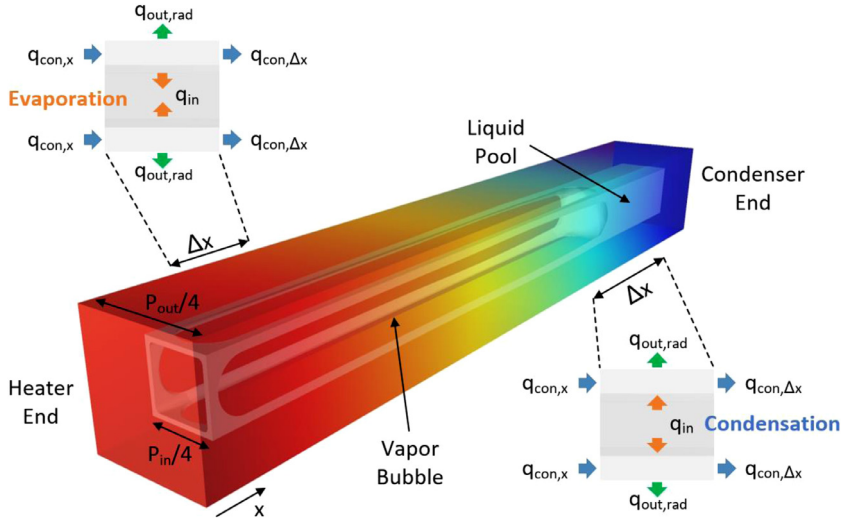


**Fig. 3.** Diagram of various heat transfer processes through the control volume of partially filled CVB module.

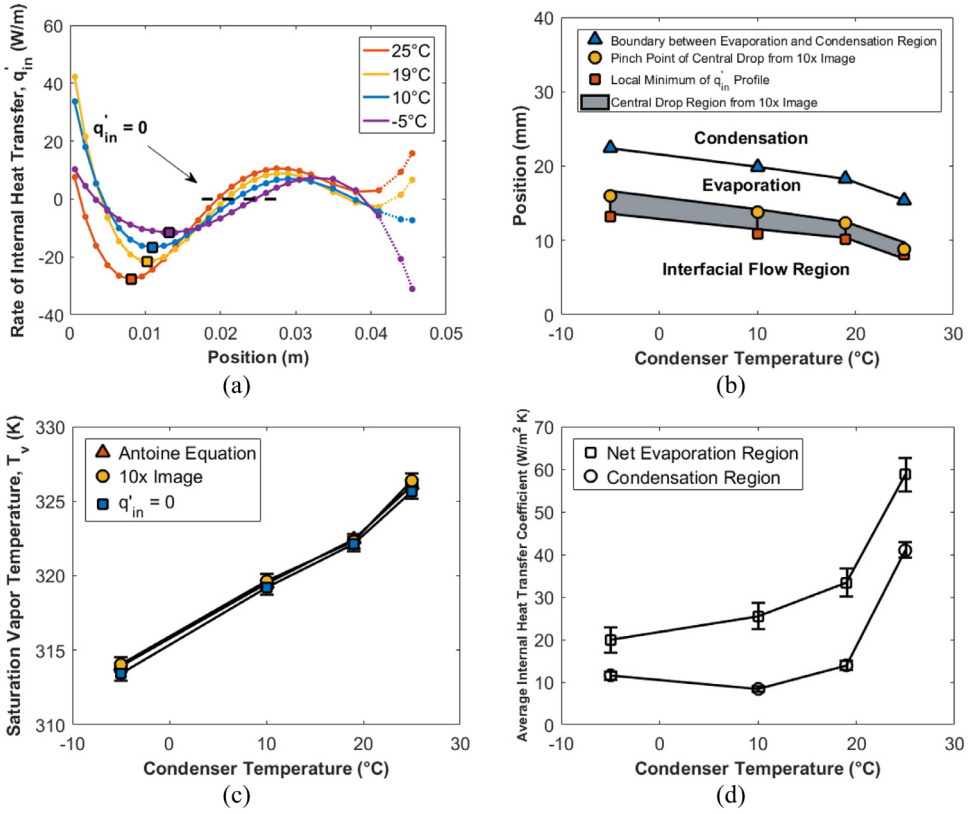


**Fig. 4.** (a) Internal heat transfer rate ($q'_{in}$) profile. The solid squares mark the local, mathematical minimum of $q'_{in}$ for each case respectively showing the maximum evaporative heat transfer. (b) The boundary positions between different regions determined from the 10× images. The central drop location was estimated using local $q'_{in}$ minimum, and it is compared with that measured from the 10× images. The span of the central drop region was measured from Fig. 2c, which is demonstrated by the white dash lines. (c) Comparison of the vapor temperatures obtained by three different approaches. (d) The average internal heat transfer coefficient, $h_{in}$, in the net evaporation region and the condensation region as a function of condenser temperature. Error bars represent the standard error of the numerical solution fitting to the experimental data for the temperature profile.

could calculate the vapor temperature in each case. This temperature should coincide with the temperature at which condensation occurs on the walls of the device.

$$T_v = \frac{B}{A - log_{10}P} - C \tag{3}$$

Here, $P$ is the vapor pressure (mmHg), and $T_v$ is the saturation vapor temperature (K). $A$, $B$, and $C$ are the Antoine equation parameters. The specific values of $A$, $B$, and $C$ for pentane as the only working fluid in the heat pipe are listed in Table 1.

The Antoine-based vapor temperature is shown in Fig. 4c and is very similar to the temperature we obtain from the one-dimensional model. Further verification of the heat transfer model involved analyzing the composite 10× micrographs from all four runs. As $T_v$ represents a saturation temperature for the vapor phase the location where the wall temperature reaches $T_v$ should indi-

**Table 1**
The Antoine equation parameters of pentane. The values are valid in the temperature range from -129.73°C to 196.5°C [11].

| Component | Antoine equation parameters ($P$ in mmHg, $T_v$ in K) | | |
|---|---|---|---|
| Pentane | $A$ | $B$ | $C$ |
| | 7.00877 | 1134.15 | 238.678 |

cate the transition from evaporation to condensation. This location is easy to see because once the wall temperature is less than $T_v$, liquid accumulates on the walls and many closely spaced interference fringes appear. Therefore, the visual observation method for checking $T_v$ took advantage of this phenomenon to locate where condensation first appeared. We then compared that position with Fig. 1b to determine the wall temperature at that location. The results for this version of $T_v$ are also shown in Fig. 4c. All three $T_v$ estimates are quite similar, so the model compares favorably with experimental observations outlining the different regions of the heat pipe.

Once $T_v$ is known, we translate from $q'_{in}$ to $h_{in}$. Our primary analysis for $h_{in}$ only considers the region from the heater wall to the point where condensation on the walls begins. A separate calculation to determine the heat transfer coefficient in the condenser region used the temperature profile from the end of the isothermal region until the point 40 mm from the heater wall. This coincided with the end of the vapor bubble. In every case, a value for the heat transfer coefficient was assumed, Eq. (1) was solved numerically, and the value for the heat transfer coefficient was adjusted to minimize the least squares error between the predicted temperature and the experimental data. Results of the average internal heat transfer coefficients in both evaporation and condensation regions at various condenser temperatures are shown in Fig. 4d. Overall, $h_{in}$ in the net evaporation region decreased as the condenser temperature decreased, in agreement with the observation that in the region near the heater end, the temperature gradient decreased with decreasing condenser temperature. In the condensation region $h_{in}$ followed a similar decreasing trend with decreasing condenser temperature. However, the -5°C case deviates from the overall trend. As the environment temperature is 21°C, the -5°C case has the longest region where the device wall temperature is lower than the temperature of the external environment and lower than the dew point on the station (~ 17 °C). Hence, radiative heat transfer switches sign near the condenser end and the cuvette surface absorbs a significant amount of heat from the environment and from vapor condensing and then freezing on the surface. Overall, both heat transfer coefficients in the evaporation and condensation region show that less heat is circulated within the device as the condenser temperature is lowered.

In the pure fluid experiment, the decrease of the average internal heat transfer coefficient is attributed to an increase in the heat transfer resistance induced by the flooding phenomenon in the interfacial flow region and to a minor extent, the increase in the overall driving force that results from decreasing the condenser temperature. As the condenser temperature decreased, the interfacial flow region grew and thereby compressed the extent of the condensation region at the same time. The effect of the condenser temperature on the average heat transfer coefficient when using pure pentane as the working fluid is opposite to the results found when using a mixture of working fluids [10,31]. In the binary mixture experiment, local pentane and isohexane compositions varied with the change of temperature and hence, with position in the heat pipe. Since each component had a different surface tension at a certain temperature and the local composition of the fluid changes with temperature, the overall surface tension of the liquid mixture stayed relatively constant in the evaporation region. The flooding phenomenon did not occur, and the interfacial flow region did not appear. Consequently, $h_{in}$ in the evaporation section increased as the condenser temperature decreased.

The interfacial flow is driven by the Marangoni stress. Using fluid property data from NIST, we approximated the change in surface tension with temperature using the linear correlation in Eq. (4). The equation is valid in the temperature range from 273 K to 463 K [37]. Based on Eq. (4), the surface tension of pentane versus the position along the main axis of the cuvette is shown in Fig. 5a.

$$\sigma_l = 0.0153076 - 0.000096\ (T - 298.15) \tag{4}$$

From Eq. (4), as the temperature drops from the heater end to the condenser end, the surface tension rises, as shown in Fig. 5a, and the Marangoni stress increases. This stress creates a flow that opposes the capillary flow from the condenser end and results in the central drop formation. In Fig. 5b, the extent of the central drop region, the pinch point location, and the predicted central drop location based on the minimum in $q'_{in}$were plotted against the surface tension gradient between the heater end and the location where condensation begins for each condenser temperature run. A linear relationship exists between the length of the interfacial flow region and the surface tension gradient as shown in Fig. 5b.

When the condenser temperature decreased, the system pressure also decreased, and the length of the interfacial flow region increased, so the starting position of condensation moves towards the condenser end. Fig. 5c summarizes the length of these three regions, which are all functions of the condenser temperature.

We focused on the performance of the heater end and the behavior of the heat transfer coefficient there because we were surprised at how strong the effect of condenser temperature was in that region and because the behavior was so much different when using a pure fluid. We compared three different sets of runs. The cooling run was the group of experiments performed at a constant heat input of 2.0 W and condenser temperatures ranging from 25°C to -5°C. The second group of experiments was a heating run where the heater power was varied from 0.8 W to 3.0 W and the condenser temperature was fixed at 19°C. The third group of experiments was another heating run where the heater input varied from 0.8 W to 2.0 W and the condenser temperature was fixed at 25°C. The full maps of the liquid-vapor distribution inside the heat pipe for the two heating groups are shown in Fig. 6 while the condenser temperature runs were shown in Fig. 2c.

The average internal heat transfer coefficients in the evaporator region were all calculated using Eq. (1) and the fitting procedure discussed previously. The Nusselt and Marangoni numbers were defined by Eqs. (5) and (6) respectively.

$$Nu = \frac{h_{in}L}{k} \tag{5}$$

$$Ma = -\frac{d\sigma_l}{dT}\frac{L}{\mu}\frac{\Delta T}{\alpha} \tag{6}$$

$L$ is defined as the characteristic length from the heater wall to the central drop position, $\Delta T$ is the temperature difference between the heater and central drop location, $d\sigma_l/dT$ is the mean surface tension variation over the temperature range defined by the slope of Eq. (4), while $\mu$ and $\alpha$ are the average values for the dynamic viscosity and thermal diffusivity respectively over the temperature range defined by $L$. The average heat transfer coefficient, $h_{in}$, is calculated using Eq. (1) for each run.

As the central drop moves away from the heater end, the Nusselt number in the net evaporation region decreases and the Marangoni number increases. In both dimensionless groups, the

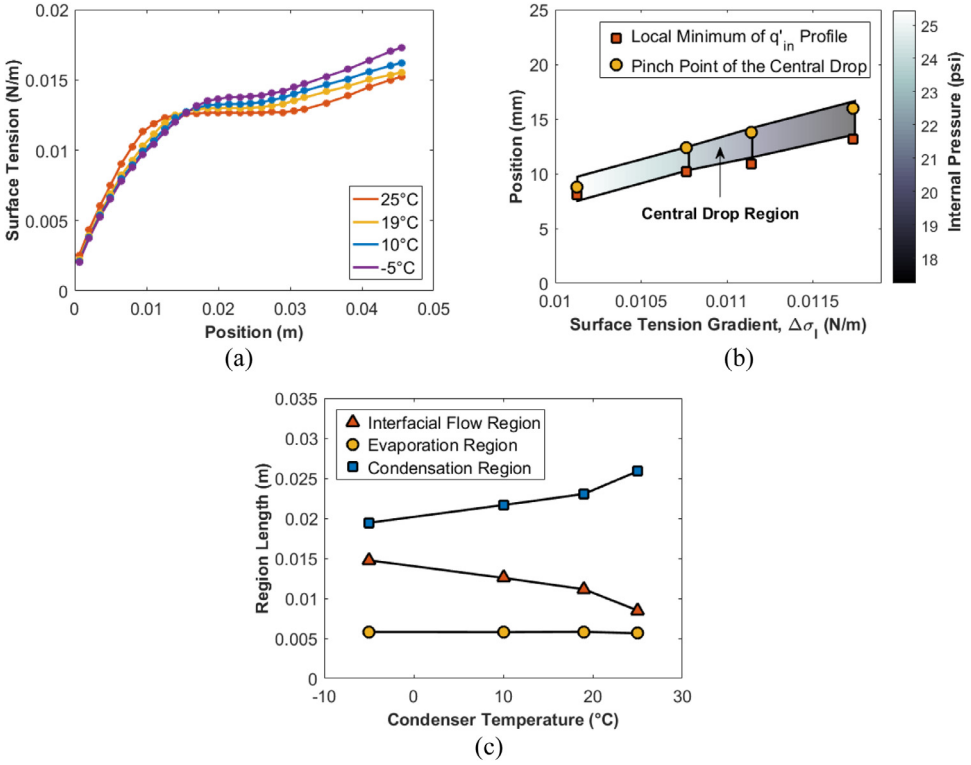


**Fig. 5.** (a) Surface tension of pentane as a function of position along the main axis of the cuvette. Error bars represent the standard error that propagates from the temperature profile. (b) The central drop location versus the surface tension gradient between the heater end and the starting location of the condensation region. The span of the central drop region was shown by the patch, and pressure variation among each case from Fig. 1c was represented by the change of the color hue. (c) The length of the interfacial flow region, evaporation region, and condensation region as a function of condenser temperature.

**Table 2**
Effect of the Marangoni stress in different experiments.

| | Thermocapillary convection around gas bubbles in pure alcohols [38] | Thermocapillary migration of Fluorinert FC-75 drops in silicone oil in microgravity [39–42] | Marangoni convection over a flat surface [43,44] | Constrained vapor bubble in microgravity |
|---|---|---|---|---|
| Experiment | 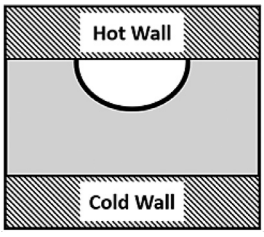  | 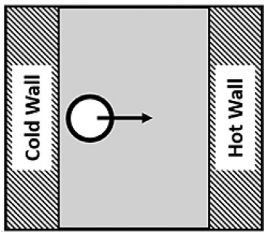  | 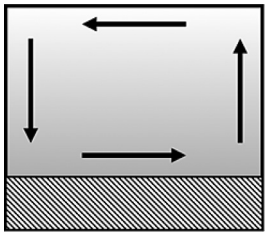 |   |
| Correlation | $Nu = f \cdot Ma^{0.333} + C$ | $U = f \cdot Ma^{-0.328}$ (Velocity as a function of Marangoni number) | $Nu = f \cdot Ma^{1/3}$ | $Nu = f \cdot Ma^{-1/3}$ |
| Contribution by the Marangoni stress | Positive | Negative | Positive | Negative |

characteristic length increases due to the longer interfacial flow region. A fit to the Nusselt number vs. Marangoni number curve collapses all the data and shows that the Nusselt number decreases with the Marangoni number to about the 1/3 power (Fig. 7).

The effect of Marangoni stresses on heat transfer has been studied under several different circumstances. Some of these findings that directly tie the Nusselt and Marangoni numbers are summarized in Table 2. Shankar and Subramanian investigated the thermocapillary migration of Fluorinert FC-75 drops in silicone oil under reduced gravity conditions [39–42]. Although heat transfer was not emphasized in the study, the velocity of the FC-75 drops as a function of the Marangoni number shares a similar exponent as in our heat pipe experiment. In a chamber with an imposed temperature gradient, the drop diameter, the temperature difference across the drop, and liquid viscosity determined the Marangoni number. The velocity of the drops decreased with increasing Marangoni number which indicates the Reynolds number decreased, and from that, we infer the Nusselt number also decreased in this situation. Most other studies focusing on heat transfer have shown a positive contribution of the Marangoni effect. Benz and Straub [38] studied a gas bubble, injected in a closed chamber filled with alcohol, where the bubble was located at the top of the chamber due to gravity. Marangoni convection around the bubble was generated by the heating and cooling plates at the top and bottom surfaces re-

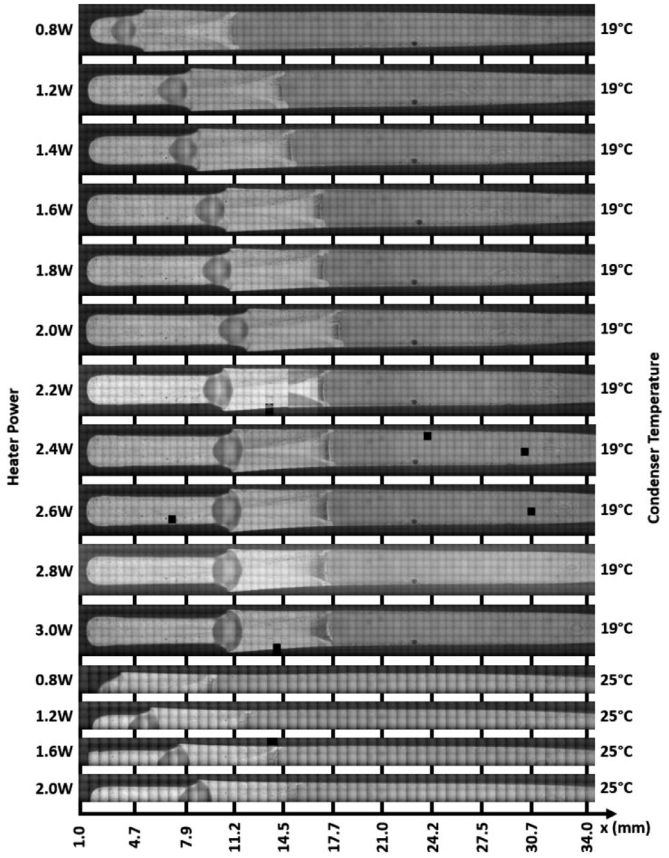


**Fig. 6.** 10× composite images of the liquid-vapor distribution for the heating groups of experiments at 19°C and 25°C condenser temperature.

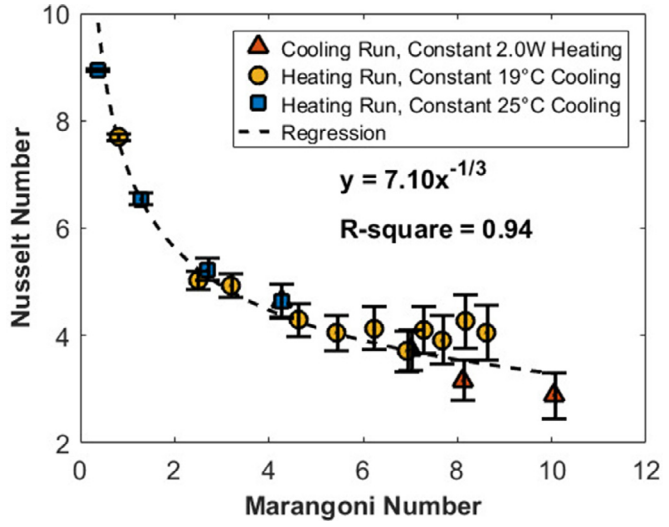


**Fig. 7.** Nusselt number as a function of the Marangoni number. The experimental data includes two groups of heating experiments and one group of cooling experiments. The fitted power equation can well present the correlation between the two quantities.

spectively. Circulation of the liquid, driven by the surface tension gradient, enhanced the heat transfer at the liquid-vapor interface. The authors fit their data to a power law and showed the Nusselt number to be a function of the Marangoni number to the 1/3 power. A similarity solution for Marangoni convection over a flat surface was analyzed by Christopher and Wang [43]. The scaling law they developed also shows that the Nusselt number should depend on the Marangoni number to the 1/3 power. In the first three groups of studies, though the contribution by the Marangoni stress is not the same, they all share a similar magnitude in the exponent, which is around 1/3. In most cases, the Marangoni flow improves the convection inside the system and assists heat transfer by augmenting the removal of the hot fluid from the surface and allowing cooler fluid to take its place. In our case, the Marangoni flow opposes the capillary return flow and so retards the heat transfer by preventing cooler fluid from reaching the hot end. Thus, while our correlation still shows a power law exponent of magnitude 1/3 in agreement with other studies, we end up with the opposite sign for the dependence.

## 3. Conclusion

The impact of the condenser temperature on heat pipe performance using pure pentane as the working fluid was investigated under microgravity conditions. In contrast with other heat pipe studies, we found that the heat pipe efficiency was degraded as the condenser temperature decreased, and this was quantified by a decrease of the heat transfer coefficient at the evaporator end. The cause was the development of a Marangoni flow that opposed the capillary return flow in the heat pipe. This created what we call an interfacial flow region where evaporation was limited. The length of the interfacial flow region increased when the condenser temperature was lowered, and the region of large-scale condensation decreased. This results in less surface area being available for condensation of the pentane vapor. Thus less condensate can be replenished to the heater end. Quantifying the Marangoni effect in the form of a heat transfer coefficient and Nusselt number at the evaporator end showed that the Nusselt number varied with the Marangoni number to the -1/3 power. The magnitude of the exponent governing the Marangoni effect agrees with other studies in the literature, but the sign of the power law dependence is opposite since, in this case, Marangoni flow prevents cooler fluid from reaching the hotter surfaces. The single correlation unifies all the data obtained in the experiments whether the condenser temperature is adjusted while the heater power remains constant or the heater power is adjusted and the condenser temperature held constant.

## Declaration of Competing Interest

The authors declare that they have no known competing financial interests or personal relationships that could have appeared to influence the work reported in this paper.

## CRediT authorship contribution statement

**Jiaheng Yu:** Writing – original draft, Formal analysis. **Thao T.T. Nguyen:** Methodology. **Anisha Pawar:** Writing – review & editing, Formal analysis. **Peter C. Wayner Jr.:** Investigation, Writing – review & editing. **Joel L. Plawsky:** Writing – review & editing, Conceptualization, Data curtion, Investigation, Supervision, Project administration. **David F. Chao:** Investigation, Conceptualization, Funding acquisition. **Ronald J. Sicker:** Project administration, Funding acquisition.

## Acknowledgments

This material is based on the work supported by the National Aeronautics and Space Administration (NASA) under grant number 80NSSC20K0120 and NSF CBET-1637816. Any opinions, findings, and conclusions or recommendations expressed in this publication are those of the authors and do not necessarily reflect the view of NASA or NSF.

## Appendix 1. Derivation of the one-dimensional heat transfer model

An energy balance was constructed based on the control volume shown in Fig. 3 of the paper.

$$q_{con,\ x} + q_{in} = \ q_{con,\ x+\Delta x} + q_{out,\ rad} \tag{A1}$$

From Fourier's law, conduction of the heat can be described by:

$$q_{con,\ x} - \ q_{con,\ x+\Delta x} = \ -kA_c\left(\frac{dT}{dx}|_x - \frac{dT}{dx}|_{x+\Delta x}\right) \tag{A2}$$

where $k$ is the thermal conductivity of the fused silica heat pipe material, and $A_c$ is the cross-sectional area of the wall, as shown in Fig. 3.

According to the Stefan–Boltzmann law, thermal radiation from the outer surface is quantified by Eq. (A3),

$$q_{rad,\ out} = \ \sigma\varepsilon P_{out}\Delta x\left(T^4 - T_\infty^4\right) \tag{A3}$$

In Eq. (A3), $\sigma$ is the Stefan–Boltzmann constant, $\varepsilon$ is the emissivity of the cuvette, $P_{out}$ is the outside perimeter of the heat pipe, $T_\infty$ represents the environment temperature, which is 21°C on average and measured by the thermocouples in the external housing where the cuvette was mounted.

The internal convective heat transfer rate and the heat exchange occurring as a result of phase change are generalized using a lumped parameter, $q_{in}$.

$$q_{in} = \ -P_{in}\Delta x\ h_{in}(T - \ T_v) \tag{A4}$$

Here, $P_{in}$ is the inside perimeter of the heat pipe, and $T_v$ is the saturation temperature of the working fluid in the vapor phase. The overall heat pipe performance in the evaporation and condensation regions is evaluated by $h_{in}$, a simple, average heat transfer coefficient. $h_{in}$ can then be used to quantify the performance under different condenser temperature conditions.

By substituting the corresponding terms in Eq. (A1) using Eq. (A2) - (A4), we obtain:

$$\begin{aligned} &- kA_c\left(\frac{dT}{dx}|_x - \frac{dT}{dx}|_{x+\Delta x}\right) - P_{in}\Delta x\ h_{in}(T - \ T_v) \\ &- \sigma\varepsilon P_o\Delta x\left(T^4 - T_\infty^4\right) = 0 \end{aligned} \tag{A5}$$

Both sides of Eq. (A5) are divided by $\Delta x$, and in the limit as $\Delta x$ approaches zero, we have:

$$-P_{in}h_{in}(T - \ T_v) + kA_c\frac{d^2T}{dx^2} \ - \sigma\varepsilon P_{out}\left(T^4 - T_\infty^4\right) = \ 0 \tag{A6}$$

Eq. (A6) can be represented in an overall sense, using the primed quantities to denote the heat transfer per unit length along the main axis:

$$q'_{in} = \ q'_{con} \ + \ q'_{out,\ rad} \tag{A7}$$

where,

$$q'_{in} = -P_{in}h_{in}(T - \ T_v) \tag{A8}$$

$$q'_{con} = -kA_c\frac{d^2T}{dx^2} \tag{A9}$$

$$q'_{out,\ rad} = \sigma\varepsilon P_{out}\left(T^4 - T_\infty^4\right) \tag{A10}$$

## References


[1] A. Faghri, Heat Pipe Science and Technology, 2nd Ed, Global Digital Press, Columbia, 2016.

[2] M. Mochizuki, T. Nguyen, K. Mashiko, Y. Saito, T. Nguyen, and V. Wuttijumnong, "A review of heat pipe application including new opportunities," vol. 2, p. 13001, 2011.

[3] L.L. Vasiliev, Heat pipes in modern heat exchangers, Applied Therm. Eng. 25 (1) (2005) 1–19 Pergamon01-Jan-.

[4] S.W. Chi, Heat Pipe Theory and Practice: A Sourcebook, Hemisphere Publishing Corporation, Washington, D.C., 1976.

[5] H. Shabgard, C.W. Robak, T.L. Bergman, A. Faghri, Heat transfer and exergy analysis of cascaded latent heat storage with gravity-assisted heat pipes for concentrating solar power applications, Sol. Energy 86 (3) (Mar. 2012) 816–830.

[6] G.P. Peterson, Overview of micro heat pipe research and development, Appl. Mech. Rev. 45 (5) (1992) 175–189.

[7] W. Srimuang, P. Amatachaya, A review of the applications of heat pipe heat exchangers for heat recovery, Renew. Sustain. Energy Rev. 16 (6) (2012) 4303–4315.

[8] H.N. Chaudhry, B.R. Hughes, S.A. Ghani, A review of heat pipe systems for heat recovery and renewable energy applications, Renew. Sustain. Energy Rev. 16 (4) (2012) 2249–2259 Elsevier Ltd.

[9] N. di Francescantonio, R. Savino, Y. Abe, New alcohol solutions for heat pipes: Marangoni effect and heat transfer enhancement, Int. J. Heat Mass Transf. 51 (25–26) (Dec. 2008) 6199–6207.

[10] T.T.T. Nguyen, A. Kundan, P.C. Wayner, J.L. Plawsky, D.F. Chao, R.J. Sicker, The effect of an ideal fluid mixture on the evaporator performance of a heat pipe in microgravity, Int. J. Heat Mass Transf. 95 (Apr. 2016) 765–772.

[11] A. Kundan, J.L. Plawsky, P.C. Wayner, Thermophysical characteristics of a wickless heat pipe in microgravity - constrained vapor bubble experiment, Int. J. Heat Mass Transf. 78 (Nov. 2014) 1105–1113.

[12] W.G. Anderson, R.W. Bonner, P.M. Dussinger, J.R. Hartenstine, D.B. Sarraf, I.E. Locci, Intermediate temperature fluids life tests - Experiments, in: Collection of Technical Papers - 5th International Energy Conversion Engineering Conference, 2, 2007, pp. 926–941.

[13] B. Saleh, G. Koglbauer, M. Wendland, J. Fischer, Working fluids for low-temperature organic Rankine cycles, Energy 32 (7) (Jul. 2007) 1210–1221.

[14] A.A. Lakew, O. Bolland, Working fluids for low-temperature heat source, Appl. Therm. Eng. 30 (10) (Jul. 2010) 1262–1268.

[15] W. Shao, Y. Zhang, Effects of film evaporation and condensation on oscillatory flow and heat transfer in an oscillating heat pipe, J. Heat Transf. 133 (4) (Apr. 2011).

[16] S. Wang, J. Chen, Y. Hu, W. Zhang, Effect of evaporation section and condensation section length on thermal performance of flat plate heat pipe, Appl. Therm. Eng. 31 (14–15) (Oct. 2011) 2367–2373.

[17] S.S. Panchamgam, S.J. Gokhale, J.L. Plawsky, S. DasGupta, P.C. Wayner, Experimental determination of the effect of disjoining pressure on shear in the contact line region of a moving evaporating thin film, J. Heat Transf. 127 (3) (Mar. 2005) 231–243.

[18] T.T.T. Nguyen, A. Kundan, P.C. Wayner, J.L. Plawsky, D.F. Chao, R.J. Sicker, Experimental study of the heated contact line region for a pure fluid and binary fluid mixture in microgravity, J. Colloid Interface Sci. 488 (Feb. 2017) 48–60.

[19] Pier.re-G.illes De Gennes, Fr.ançoise Brochard-Wyart, Da.vid Quéré, Capillarity and Wetting Phenomena: Drops, Bubbles, Pearls, Waves, Springer Science & Business Media, Berlin, 2013.

[20] A.W. Adamson, A.P. Gast, J. Wiley, Physical Chemistry of Surfaces, 6th Ed, Wiley-Interscience, Hoboken, 1997.

[21] M.M. Weislogel, Capillary flow in interior corners: the infinite column, Phys. Fluids 13 (11) (Nov. 2001) 3101–3107.

[22] J. Bico, D. Quéré, Rise of liquids and bubbles in angular capillary tubes, J. Colloid Interface Sci. 247 (1) (Mar. 2002) 162–166.

[23] S. Son, L. Chen, Q. Kang, D. Derome, J. Carmeliet, Contact angle effects on pore and corner arc menisci in polygonal capillary tubes studied with the pseudopotential multiphase lattice Boltzmann model, Computation 4 (1) (Feb. 2016) 12.

[24] A. Faghri, S. Thomas, Performance characteristics of a concentric annular heat pipe: part I-experimental prediction and analysis of the capillary limit, J. Heat Transf. 111 (4) (Nov. 1989) 844–850.

[25] R. Savino, D. Paterna, Marangoni effect and heat pipe dry-out, Phys. Fluids 18 (11) (2006).

[26] C.P. Migliaccio, H.K. Dhavaleswarapu, S.V. Garimella, Temperature measurements near the contact line of an evaporating meniscus V-groove, Int. J. Heat Mass Transf. 54 (7–8) (Mar. 2011) 1520–1526.

[27] H.B. Ma, G.P. Peterson, The minimum meniscus radius and capillary heat transport limit in micro heat pipes, J. Heat Transf. 120 (1) (1998) 227–233 American Society of Mechanical Engineers Digital Collection01-Feb-.

[28] B. Suman, N. Hoda, Effect of variations in thermophysical properties and design parameters on the performance of a V-shaped micro grooved heat pipe, Int. J. Heat Mass Transf. 48 (10) (May 2005) 2090–2101.

[29] L. Yang, G.M. Homsy, Steady three-dimensional thermocapillary flows and dry-out inside a V-shaped wedge, Phys. Fluids 18 (4) (2006).

[30] M. Markos, V.S. Ajaev, G.M. Homsy, Steady flow and evaporation of a volatile liquid in a wedge, Phys. Fluids 18 (9) (Sep. 2006) 092102.

[31] T.T.T. Nguyen, A. Kundan, P.C. Wayner, J.L. Plawsky, D.F. Chao, R.J. Sicker, Effects of cooling temperature on heat pipe evaporator performance using an ideal fluid mixture in microgravity, Exp. Therm. Fluid Sci. 75 (2016) 108–117.

[32] W.J. Bowman, D. Maynes, Comparison of standard and heat-pipe fins with specified tip temperature condition, J. Thermophys. Heat Transf. 15 (1–4) (2001) 421–426.

[33] A. Kundan, T.T.T. Nguyen, J.L. Plawsky, P.C. Wayner, D.F. Chao, R.J. Sicker, Condensation on highly superheated surfaces: unstable thin films in a wickless heat pipe, Phys. Rev. Lett. 118 (9) (Mar. 2017).

[34] A. Kundan, et al., Thermocapillary phenomena and performance limitations of a wickless heat pipe in microgravity, Phys. Rev. Lett. 114 (14) (Apr. 2015).
[35] A. Kundan, J.L. Plawsky, P.C. Wayner, Effect of capillary and marangoni forces on transport phenomena in microgravity, Langmuir 31 (19) (2015) 5377–5386.
[36] A. Kundan, T.T.T. Nguyen, J.L. Plawsky, P.C. Wayner, D.F. Chao, R.J. Sicker, Arresting the phenomenon of heater flooding in a wickless heat pipe in microgravity, Int. J. Multiph. Flow 82 (2016) 65–73.
[37] P. Linstrom and W. Mallard, "NIST Chemistry webbook; NIST standard reference database," 2001.
[38] J. Betz, J. Straub, Numerical and experimental study of the heat transfer and fluid flow by thermocapillary convection around gas bubbles, Heat Mass Transf. und Stoffuebertragung 37 (2–3) (Apr. 2001) 215–227.
[39] R. Balasubramaniam, C.E. Lacy, G. Woniak, R.S. Subramanian, Thermocapillary migration of bubbles and drops at moderate values of the Marangoni number in reduced gravity, Phys. Fluids 8 (4) (Apr. 1996) 872–880.
[40] R. Balasubramaniam, R.S. Subramanian, Thermocapillary bubble migration - thermal boundary layers for large Marangoni numbers, Int. J. Multiph. Flow 22 (3) (Jun. 1996) 593–612.
[41] R. Balasubramaniam, J.E. Lavery, Numerical simulation of thermocapillary bubble migration under microgravity for large reynolds and marangoni numbers, Numer. Heat Transf. Part A Appl. 16 (2) (1989) 175–187.
[42] P.H. Hadland, R. Balasubramaniam, G. Wozniak, R.S. Subramanian, Thermocapillary migration of bubbles and drops at moderate to large Marangoni number and moderate Reynolds number in reduced gravity, Exp. Fluids 26 (3) (1999) 240–248.
[43] D.M. Christopher, B. Wang, Prandtl number effects for Marangoni convection over a flat surface, Int. J. Therm. Sci. 40 (6) (Jun. 2001) 564–570.
[44] D. Schwabe, J. Metzger, Coupling and separation of buoyant and thermocapillary convection, J. Cryst. Growth 97 (1) (Sep. 1989) 23–33.